Momentum flux characteristics of vertical propagating Gravity Waves

Prosper K. Nyassor[1], Cristiano M. Wrasse[1], Igo Paulino[2], Cosme A. O. B. Figueiredo[2], Ricardo A. Buriti[2], Hisao Takahashi[1], Delano Gobbi[1], and Gabriel A. Giongo[1]

[1]Space Weather Division, National Institute of Space Research (INPE), São José dos Campos, Brazil
[2]Academic Unit of Physics, Federal University of Campina Grande (UFCG), Campina Grande, Brazil

Correspondence: Prosper K. Nyassor (prosper.nyassor@inpe.br)

Abstract. Simultaneous observations of airglow intensity, rotational temperature, and wind data at São João do Cariri (36.31°W; 07.40°S) by Co-located photometer, all-sky imager, and meteor radar were used to study the characteristics of vertical propagating gravity waves (GWs). Using the photometer data, the phase progression of GWs with the same propagation period in the OI 557.7 nm, O_2, NaD-line, and OH (6-2) emission layers were then used to determine the upward or downward vertical propagation of the waves. The vertical phase speed and wavelength are estimated using the wave period and phase difference at different altitude. From the O_2 and OH (6-2) rotational temperatures, the total energy and the momentum flux of the downward propagating GWs were determined. For the upward propagating GW only the momentum flux and potential energy were estimated due to lack of observed wind. Further analysis of the momentum flux for each of the two events revealed that the momentum flux and potential energy of the downward propagating GWs increases with decreasing altitude. On the contrary, the GW momentum and energy of the upward propagating waves increases with increasing altitude. Thus, clearly demonstrating the transfer of momentum flux and energy from the source to the sink. This characteristic difference can be used to careful analysis the changes in GWs energy propagation due to reflection of non-primary GWs.

1 Introduction

The vertical propagation of atmospheric gravity waves (GWs) is known to be the main transport mechanism of momentum and energy into the upper atmosphere (Fritts and Alexander, 2003). Owing to the decrease of density with altitude, amplitudes of GWs increase exponentially if dissipation/wave breaking did not occur. GWs are excited by flows surging up mountains (e.g., Gossard and Hooke, 1975; Lindzen, 1984), fronts and jet streams (e.g., Lindzen, 1984; Fritts and Alexander, 2003), convective layers (e.g., Townsend, 1966), deep convection thunderstorms (e.g., Taylor and Hapgood, 1988; Fritts and Alexander, 2003; Sentman et al., 2003; Yue et al., 2009; Vadas et al., 2009; Nyassor et al., 2021, 2022a, b), volcanoes (e.g., Yue et al., 2022; Figueiredo et al., 2023), typhoons (e.g., Li et al., 2022; Chou et al., 2017), by earthquakes (e.g., Heale et al., 2020), solar

eclipses (e.g., Paulino et al., 2020, and references therein) and other process that cause unbalance between the gradient of pressure and the buoyancy. The waves then propagate both horizontally and vertically (Becker and Schmitz, 2003).

Vertical propagation characteristics of gravity waves are controlled by background temperature and wind relative to the horizontal phase speed of waves. Depending on wave interaction with the background field, the waves can be classified as a ducted, propagating, or evanescent modes (Gossard and Hooke, 1975). Some of these waves suffer critical level filtering when propagating waves encounter an equal vector of background wind, where the wave can be absorbed by the background Heale and Snively (2015). Otherwise, it can be reflected if the gravity wave encounters a strong wind in the opposite direction. According to Fritts and Alexander (2003), reflected waves from the upper and (or) lower altitude regions can be (partially) ducted. GWs are filtered in the middle and lower thermosphere (MLT) region during breaking. Vertical propagating waves interact with the mean flow through the transfer of momentum and energy dissipation when breaking (Lindzen, 1981; Holton, 1982), particularly in the mesosphere. Thus, these waves significantly contribute to atmospheric circulation and dynamical fields of temperature and wind (Le Du et al., 2022).

Horizontal and vertical propagation of GWs are greatly influenced by the background wind and temperature fields (Nappo, 2013). The background fields can either hinder or favor the vertical propagation of the wave. Doppler or thermal ducts favor longer horizontal propagation of GWs (Bageston et al., 2011; Snively et al., 2007; Snively and Pasko, 2008) whereby hindering the vertical propagation. Vertical propagating GWs can either be upward (vertical wavenumber lower than zero, $m < 0$) or downwards ($m > 0$), where energy and momentum are transported in either direction. A typical example is the vertical propagation of secondary GWs which resulted from primary GWs breaking and/or dissipation in the MLT (Vadas et al., 2003). During the breaking/dissipation of primary GW, energy and momentum are released, which are further transported upward and downward as they propagate (Vadas et al., 2003).

Several observational techniques (e.g., Suzuki et al., 2013) have been employed to study the vertical propagation of GWs. Observation techniques such as Lidar (Suzuki et al., 2013), radiosonde (Schöch et al., 2004; Sato and Yoshiki, 2008; Yamashita et al., 2009) among others, have been used. In the mesosphere, Nyassor et al. (2018) an airglow photometer are used to study the vertical propagation of GWs. According to Nyassor et al. (2018, and references therein), simultaneous observation of multiple airglow emissions is one of the techniques used to investigate the vertical propagation of gravity waves in the mesosphere. This technique is possible if and only if the vertical wavelengths of the wave are larger than the thickness of the airglow emission layer (Nyassor et al., 2018, and references therein). Such observational data can be used to determine the propagation characteristics and amplitude growth of gravity waves (Taori et al., 2005).

In this research, the characteristics of the momentum flux and energy of vertical (upward and downward) propagation of GWs are examined. This work is conducted using principally a data from a multi-airglow photometer observations similar to the work of Nyassor et al. (2018). Observations of GWs propagating through the emissions: atomic oxygen green line (OI 557.7 nm), molecular oxygen (O$_2$ - 864.5 nm), sodium D-line (NaD-589.0 nm), and hydroxyl (OH) (6 - 2) band. GWs with the same period propagating through all the four (4) emission layers were selected for this study. Using complementary observations from co-located all-sky imager and meteor radar, the characteristics of GW energy and momentum flux with altitude are explored. As, the characteristics of GW energy and momentum flux of upward propagating waves are well known and explored, little has

been done so far on downward propagating wave, thus their characteristics needs further investigation. As density increases with decreasing altitude, this work intends to study how the characteristics of the GWs energy and momentum flux vary for the downward propagating waves.

2 Observation and data analysis

2.1 Airglow Photometer

The airglow photometer used in the observation of the mesospheric airglow emissions: OI 557.7 nm, O_2 (0 - 1), NaD Line, and OH (6 - 2) is located at São João do Cariri (36.31°W; 07.40°S). The photometer is a multi-channel tilting filter photometer (Multi-3) with five interference filters. The background continuum intensity (R nm^{-1}) and the line intensity (R) were measured to obtain the zenith sky spectrum by tilting the filters relative to their optical axes in which a scan of a wavelength of about 8 nm was made. The mesospheric component of the OI 557.7 nm was estimated by removing the effect of the simultaneous observation of OI 630.0 nm intensity in the ionospheric F-region component computed as 20% (Silverman, 1970). The temporal resolution of the observation is 2 minutes, thus GWs with periods greater than 2 minutes can be observed. The photometer characteristics, that is, calibration scheme and error, spectral resolution, and sensitivity, can be seen in Nyassor et al. (2018, and references therein).

An observation scheme of 13 nights per month centered around the time of the new moon was made with more than 6 h of continuous observation time per night. The observational data used for this study extend from January 2000 to December 2007, which resulted in a total of clear sky observation nights of 1051. Details on the Multi-3 filter photometer can be found in Wrasse et al. (2004) and references therein. The database of OI 557.7 nm, O_2, NaD-Line, and OH (6 - 2) was analyzed to find GWs propagating with same period in each emission altitude. Among the total nights of clear sky night observation, 389 nights present similar periods in at least two emission layers, of which 24 nights present similar periods in three emission layers. For this study, 2 GW events with the same period in all the 4 emission layers are selected. The photometer is used for airglow intensity observation and for the rotational temperature of the O_2 (0 - 1) and OH (6 - 2) emission layers (Buriti et al., 2001).

2.1.1 Atmospheric Bands Rotational Temperatures derived from OH (6 - 2) Meinel and O_2 (0 - 1)

Due to the Doppler broadening attained by the OH rotational line spectrum, it is possible to measure the mesopause temperature. The collision frequency of OH with the neutral atmosphere near 90 km of altitude has been shown to be of the order of $10^4 \ s^{-1}$ with a lifetime of the excited OH being around 3 - 10 ms (Mies, 1974). This indicates that the excited OH molecules in the rotational energy levels are in thermal equilibrium with the atmospheric ambient gas (Sivjee and Hamwey, 1987; Takahashi et al., 1998) and thus, a good proxy for atmospheric temperature studies. The OH rotational line spectra is an open structure with separation of 1 - 2 nm between the lines, which makes it easy to measure individual lines with a low resolution (of ∼1 nm) spectrometer. Further, the line intensities of most of the bands are only a function of the rotational temperature. Thus, using two lines from a single band, the rotational temperature can be estimated using the following equation Mies (1974):

$$T_{n,m} = \frac{E_{\nu'}(J'_m) - E_{\nu'}(J'_n)}{k_B In\left[\frac{I_n}{I_m}\frac{A(J'_m,\nu'\rightarrow J''_{m+1},\nu'')}{A(J'_n,\nu'\rightarrow J''_{n+1},\nu'')}\frac{2J'_m+1}{2J'_n+1}\right]},\tag{1}$$

where, $T_{n,m}$ is the rotational temperature estimated from two intensity lines, I_n and I_m, from rotational levels J'_n, J'_m in the upper vibrational level ν', to J''_{n+1}, J''_{m+1} in the lower vibrational level ν''. $E_\nu(J)$ is the energy of the level (J,ν). $A(J'_n,\nu' \rightarrow J''_{n+1},\nu'')$ is the Einstein coefficient, for the transition from J'_n,ν' to J''_n,ν''. k_b is the Boltzmann Constant.

In this studies the OH (6 - 2) band is used. Molecular oxygen also satisfies the local thermal equilibrium (LTE) similar to OH bands, which makes it possible for the estimation of the rotational temperature. O_2 is known to have a lifetime of more that $\sim 10\,\text{sec}$, making it capable of attaining the LTE. The rotational temperature can also be determined using a similar procedure of OH rotational temperature.

2.2 Meteor Radar

Background winds from a SKiYMET all-sky interferometric meteor radar with a two-element receiving and three-element transmitting antenna were used to observe mesospheric winds. The meteor radar operates at the same location of the photometer. This radar operates at a frequency of 35.24 MHz with a maximum transmitter power of 12 kW. The respective temporal and vertical resolutions of this radar are typically 60 min and 1 km. The observation characteristics of the radar have been published elsewhere in Nyassor et al. (2018, and references therein).

2.3 All-Sky Imager

An all-sky imager in São João do Cariri was used to determine the horizontal component of the GWs observed by the photometer. Images of OH (6 - 2), O_2 (0-1), OI 557.7 nm, and OI 630.0 nm airglow emission layers were taken by this equipment. With regard to this work, only the OH (6-2) and O^2 (0 - 1) bands airglow images corresponding to the selected coincident photometer observation were used. The airglow all-sky imager is an optical instrument made of a fast fish-eye (f/4) lens, a telecentric lens system, a filter wheel, and a charged coupled device (CCD) camera. The CCD camera has an area of $6.04\,\text{cm}^2$ with a 1024×1024 back-illuminated pixel array of 14 bits per pixel. In order to enhance the signal-to-noise ratio, the images were binned on chip down to a resolution of 512×512. The high quantum efficiency, low dark noise (0.5 electrons pixel^{-1}s^{-1}), low readout noise (15 electron rms), and high linearity ($0.05\,\%$) of this device enable it to measure airglow emissions (Nyassor et al., 2018).

3 Methodology and Data Analysis

3.1 Photometer Time Series

The methods to obtain the final result of the photometer data include (i) preprocessing, (ii) processing, (iii) parameterization, and (iv) discussion. A graphical demonstration of these procedures is shown in the flowchart in Figure 1.
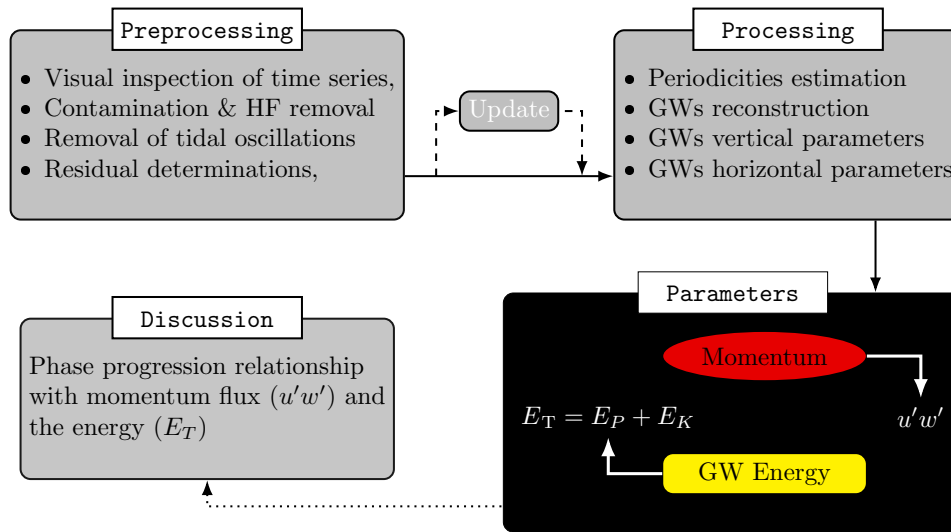
Figure 1. Flowchart showing airglow photometer data processing procedures and GW characterization. The procedure includes preprocessing, processing, parameterization, and discussion.

3.2 Preprocessing

This preprocessing stage involves four steps, as outlined in Figure 1. Firstly, the time series is made up of the variations of wave oscillations and those due to contaminants. Hence, there is a need for visual inspection to detect any of these contaminants that appear as spikes in the time series. The contaminants can be due to artificial light sources, clouds, or astronomical lights passing across the field of view of the photometer. In Figure 2, the hours are in universal time (UT) and span from 18:00 UT on 04 December 2004 to 28 (04:00 UT) on 05 December 2004. In Figure 2(a), a typical spike due to contaminant is highlighted in red. Also, gaps are usually found in the data due to instrumental problems (however, no gaps exist for this data). A criterion is set such that if the gaps or spikes in the data set are interrupted frequently in order of minutes, the data set will be disregarded. Spikes are removed from the dataset. If the clean data (data without spikes) has a continuous observation for less than 3 hours, the event is disregarded. Due to the spike in the time series in Figure 1a, the data is limited to 19 - 25 hours.

Clean time series with continuous observations of more than 3 hours are considered for further analysis. Next, high frequency oscillations are removed by applying a three-point running mean. Figure 2b shows the clean and smooth (three-point averaged) data. Finally, to obtain a dataset with only GW oscillations since GWs are modulated by tides, a harmonics for semidiurnal and terdiurnal tides is constructed using Equation 2 (red solid line in Figure 2(c)).
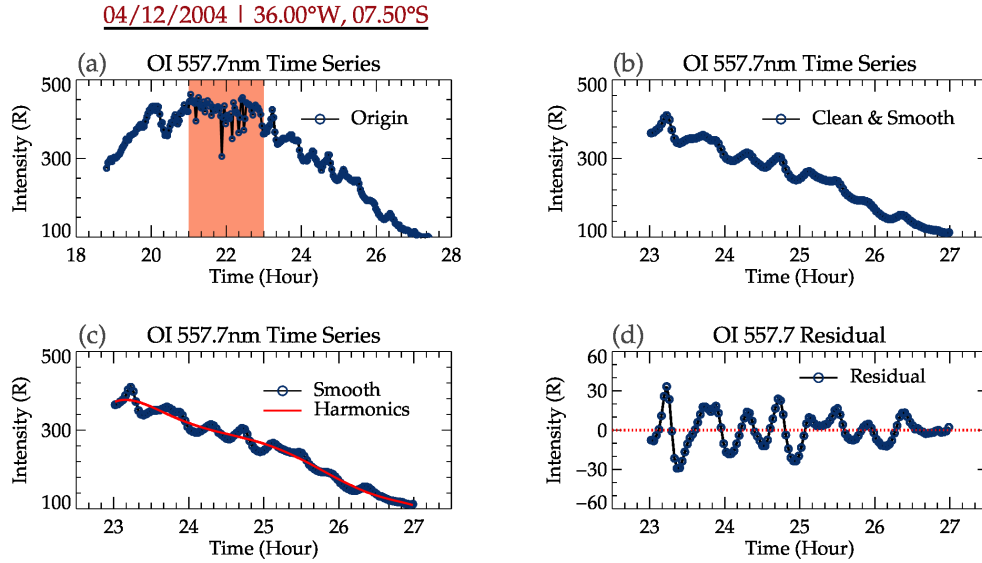
Figure 2. A step-by-step procedure of the preprocessing stage of a photometer data. Panel (a) is the original OI 557.7 nm time series. In panel (b), the clean and smooth time series is presented. The harmonics of tides, semidiurnal and terdiurnal (red solid line), are constructed and shown in panel (c). The residual (difference between the harmonics and clean-smooth) in (c) is shown in panel (d).

The harmonic is subtracted from the smoothed time series to obtain a time series of the residual (purely GWs). The residual is then used to investigate the vertical propagation of GWs.

$$Y = A + B_i cos\left(\frac{2\pi(x - \phi_i)}{\tau_i}\right) \tag{2}$$

where A and B_i are the unknown amplitude, x is the observation time series, ϕ_i is the phase, and τ_i is the period. i represent the number of periods, which in this case is the periods of semidiurnal ($\tau = 12\,hrs$) and terdiurnal ($\tau = 8\,hrs$).

3.3 Processing

In the processing stage, Lomb-Scargle periodogram and Wavelet analysis were used to determine the dominant periods in the time series of each emission layer. At least a dominant peak is chosen and used to reconstruct new harmonics and over plotted on the residual. The new harmonics is then normalised and plotted in order of increasing altitude, i.e., 87, 89, 92, and 95 km. Note that the rotational temperature of OH (6 - 2) and O_2 were also subjected to the Lomb-Scargle and Wavelet analysis. From the normalized time series arranged according to their altitude, the phases (ϕ) of the GWs at each altitude were determined. Using the differences in the phase and altitude between each of the two consecutive emission layers, the average vertical wavelength (λ_z) of the wave is given by Nyassor et al. (2018)

$$\lambda_z = \frac{V_z}{\tau}, \tag{3}$$

where $V_z = \Delta d/\Delta\phi$ is the vertical velocity, with Δd being the difference between the higher and lower emission layers and their respective phases $\Delta\phi$ and τ is the period. A typical result obtained from the procedures in the processing stage is presented in Figure 3.
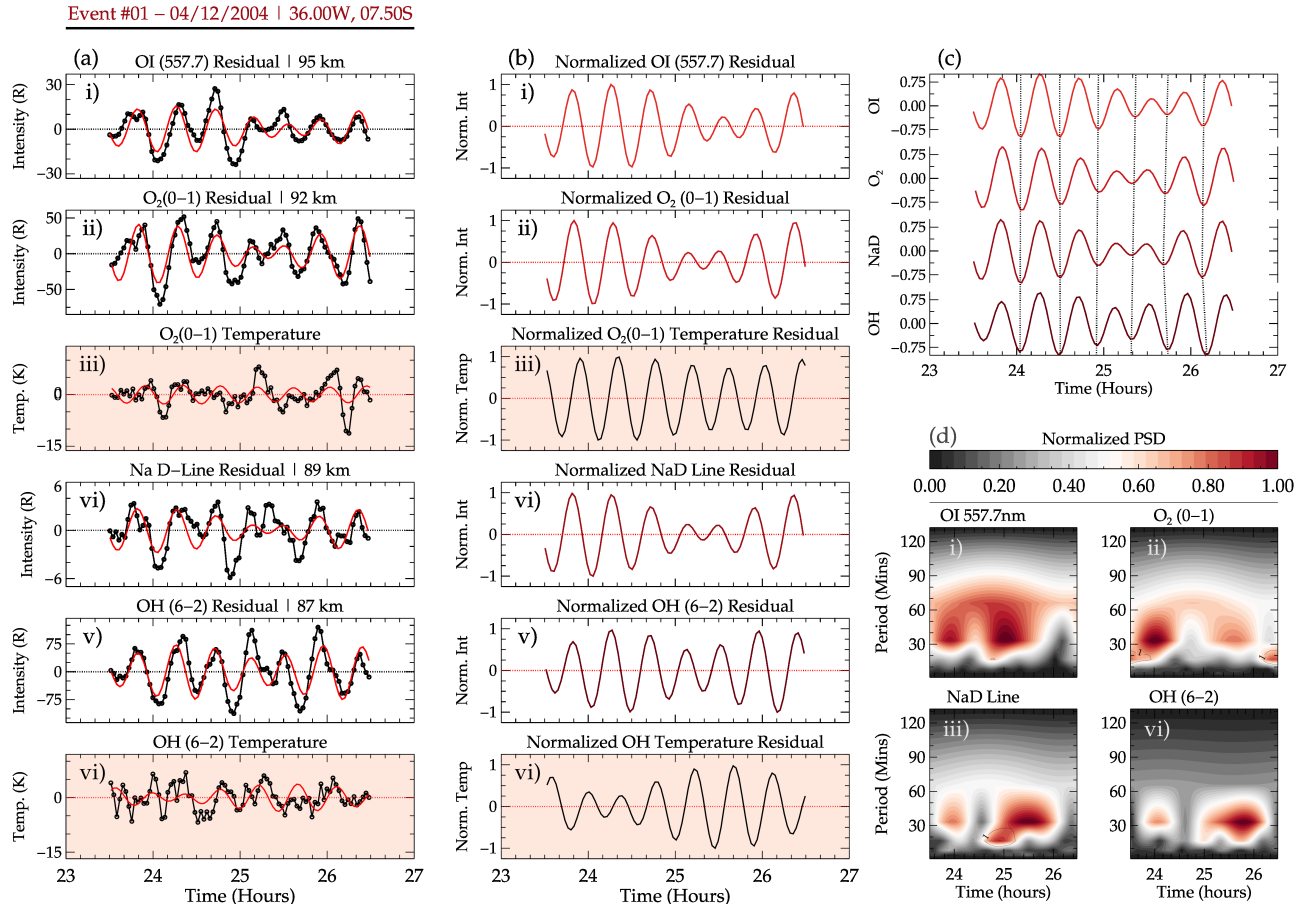
Figure 3. The detailed description of the processing stage of the preprocessed data (obtained form Figure 2). The reconstructed harmonics of the gravity wave oscillations (red solid line) using the dominant periods determined by Wavelet analysis and Lomb-Scargle periodogram, and the residuals for each airglow emission layer and those with their rotational temperature are presented in panel (a). The corresponding normalized residuals are shown in panel (b). Using the normalized residuals in panel (c), the phase propagation of the gravity wave oscillation at each emission layer altitude is determined using the vertical slanted dotted lines. In panel (d), the Wavelet analysis result of each emission layer is shown.

After the residual time series was determined, the periodicities were calculated. For these residuals, the dominant period are 25.47 min and 33.47 min. Using these periods and Equation 2, the signals (black solid line with open circle) for each emission layer is reconstructed (red solid line) as shown in panel (a) of Figure 3. Unlike Figure 2, the residuals of all the emission layers are plotted, including the rotational temperatures of OH (6 - 2) and O_2 (0 - 1). The rotational temperatures are presented

150 in the plots with red background in panels (a.iii) and (a.vi) of in Figure 3. In panels (b.i) - (b.vi) of Figure 3, the normalized reconstructed residual for each emission layer (including the rotational temperatures of OH(6-2) and O_2) (0 - 1) is presented.

From the reconstructed time series, it is clear that all the emission layers are similar, indicating that the same GWs propagate through these layers. It is worth mentioning that the time series of the rotational temperature has also been subjected to all the above mentioned procedures to confirm that similar wave packets observed in the intensity are also present in the temperature.

155 In panel (c), the normalized reconstructed time series intensity is plotted in ascending order of altitude, from which the phase progression of the waves with altitude is determined. Using the dotted vertical lines, the phase progressions are determined. The periods determined using Wavelet analysis is presented in Figure 3(d). It is observed that there is a strong presence of range of wave periods between 30 mins to 90 mins in all the four (4) emission layers. The plots in panel (d) are normalized to standardize the variations of the individual emission layers with the scale defined in the color bar. With these parameters, the

160 momentum flux and the total energy of the wave at the emission layers of OH (6 - 2) and O_2 (0 - 1) are estimated.

3.4 Parameters

In the parameter stage, the total energy (E_T), that is, the sum of the potential (E_p) and kinetic (E_k) energies and momentum flux ($u'w'$) of the GWs were estimated. The total energy is given by

$$E_T = E_p + E_k$$
$$E_p = \frac{1}{2}\left(\frac{g}{N}\right)^2\left(\frac{T'}{\overline{T}}\right)^2 \tag{4}$$
$$E_k = \frac{1}{2}\left(u'^2 + v'^2\right),$$

165 where g is the gravitational accelerations, N is the Brünt Väisäla frequency, T' is the GWs perturbations, $\overline{T}$ is the background temperature, u' is the zonal wind GW perturbation and v' is the meridional wind GW perturbations (Wang and Geller, 2003). The upper term of Equation 4 is the total energy (E_T), whereas the middle and bottom terms are the potential (E_p) and kinetic (E_k) energies. The Brünt Väisäla frequency is defined as

$$N = \left(\frac{g}{\theta}\frac{d\theta}{dz}\right)^{1/2}, \tag{5}$$

170 where $\theta = T\left(P/P_0\right)^{R/c_p}$ is the potential temperature with p and p_o being pressure and reference pressure, respectively. R is the gas constant, and the c_p is the heat capacity at constant pressure.
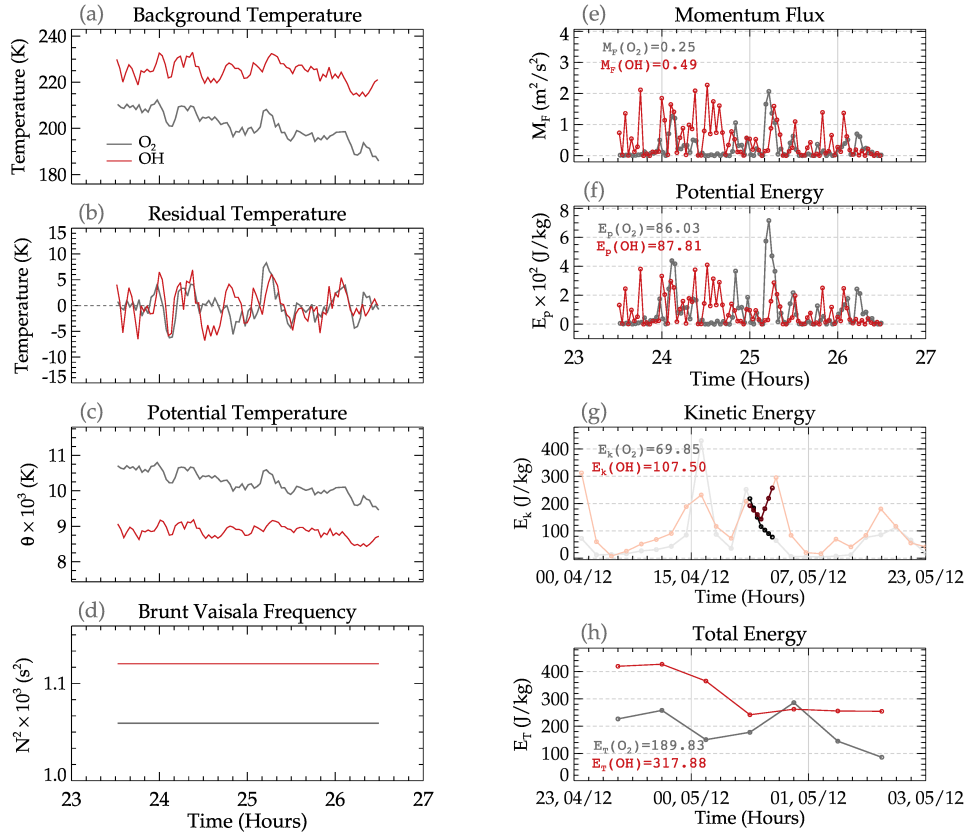
Figure 4. The parameter stage of the methodology is presented. Panels (a), (b), (c), and (d) present the time series of the background temperature, residual temperature, potential temperature, and Brünt Väisälä frequency, respectively. The time series of the momentum flux (M_F), potential energy (E_p), kinetic energy (E_k), and total energy ($E_T = E_p + E_k$) of the gravity waves at the O$_2$ and OH emission altitudes are presented in panels (e), (f), (g), and (h), respectively.

The zonal and meridional momentum fluxes of the gravity waves is determined by adapting the approach of Vargas et al. (2009), that is, given by

$$M_{Fzon}/\rho_0 = \langle u'w' \rangle = -\frac{1}{2} \frac{km\omega^2}{k_H^2} \frac{g^2}{N^4} \left(\frac{T'}{\overline{\overline{T}}} \right)^2$$
$$M_{Fmer}/\rho_0 = \langle v'w' \rangle = -\frac{1}{2} \frac{lm\omega^2}{k_H^2} \frac{g^2}{N^4} \left(\frac{T'}{\overline{\overline{T}}} \right)^2,$$

(6)

175   where ρ_0 is the density at the emission layers, $k_H^2 = k^2 + l^2$ is the horizontal wavenumber with k and l being the zonal and meridional wavenumbers, m is the vertical wavenumber, ω is the intrinsic frequency, g is the gravitational acceleration and

N the Brünt Väisälä frequency. The $T'/\overline{T}$ is the relative temperature perturbation, and T' is the GWs induced temperature variation, and $\overline{T}$ is the background temperature. The total momentum flux (M_F) of the GW is given by

$$M_F/\rho_0 = \langle u'w' \rangle = -\frac{1}{2}\frac{\omega^2}{k_H}\frac{g^2}{N^4}\left(\frac{T'}{\overline{T}}\right)^2, \tag{7}$$

180   Estimating the total energy (E_T) and the momentum flux (M_F) of GWs depends on observed temperature and wind data. As mentioned earlier, rotational temperature from photometer observations were used for M_F and E_p, whereas for the E_k, the meteor radar winds were used. In Figure 4, the time series of the O_2 and OH rotational temperature is shown in panel (a). In panel (b), the residual temperature (the GW perturbation) are shown, while in panels (c) and (d), the estimated potential temperatures (θ) and the square of Brünt Väisälä frequency (N^2) are presented. Time variation of the momentum flux (M_F),

185   potential (E_p), kinetic (E_k), and total (E_T) energies at the O_2 and OH emission layer altitudes are shown in panels (e), (f), (g) and (h), respectively.

Since the meteor radar wind has a temporal resolution of one (1) hour, E_k at each hour was determined and presented in a contour plot in Figure A1 in Appendix A to have a general characteristic. The E_k was then interpolated to obtain a thirty (30) minutes temporal resolution. Also, the vertical resolution in altitude was interpolated to 1 km vertical resolution. The 1 hr $\times$

190   1 km E_T variation at the O_2 and OH (6 - 2) emission layer altitudes are plotted in Figure 4 (g and h). The GW wind variation at the emission layer altitudes of O_2 and OH are marked by the horizontal dashed lines in panels (c) and (d) of Figure A1.

To determine the horizontal parameters of the selected events, images from co-located all-sky imager at the São João do Cariri were used. The spectral analysis technique described in Wrasse et al. (2024) was used to determine the horizontal wavelength (λ_H), period (τ_H), phase speed (c_H), and propagation direction (ϕ_H) using the keogram technique (Figueiredo

195   et al., 2018; Wrasse et al., 2024). From the horizontal wavelength, the zonal (k) and meridional (l) wavelength numbers were determined and used in Equations 6 and 7 to estimate the momentum flux. An important condition considered in the selection of the horizontal propagating GWs is that the period must be equal or similar to the period of the vertical component observed in the photometer data. A summary of the keogram analysis and a sample result are shown in Figure A2 in Appendix A.

4   Results

200   The results of two (2) selected cases obtained from Section 3 are presented in this section. In Figure 5, the result of the selected events are presented. Events one (#01) and two (#02) occurred on 04 December 2004 and 21 May 2006 at São João do Cariri are presented, respectively. In Figure 5(a and b), the 04 December2004 event reconstructed gravity wave oscillation of similar periods propagating through OI 557.7 nm, O_2 (0 - 1), NaD line and OH (6 - 2) and their periodicities are presented, respectively. The dominant periods used in the reconstruction of the waves of these events are 00.42 hr (25.47 min) for all the emission layers

205   and 00.50 hr (30.29 mins) for IO 557.7 nm, O_2 (0-1) and NaD. However, the period of the OH (6 - 2) was 0.55 hr (33.47 min). From the phase propagation, an upward phase propagation, indicated by the first four black vertical dashed lines, was observed. For the two red dashed lines, an upward phase propagation was observed between the emission layers of OI 557.7 nm, O_2 (0-1)

and NaD line. A downward phase propagation was observed between NaD line and OH (6 - 2). The turning point of the phase lines of the red dashed lines is highlighted by the light red background.
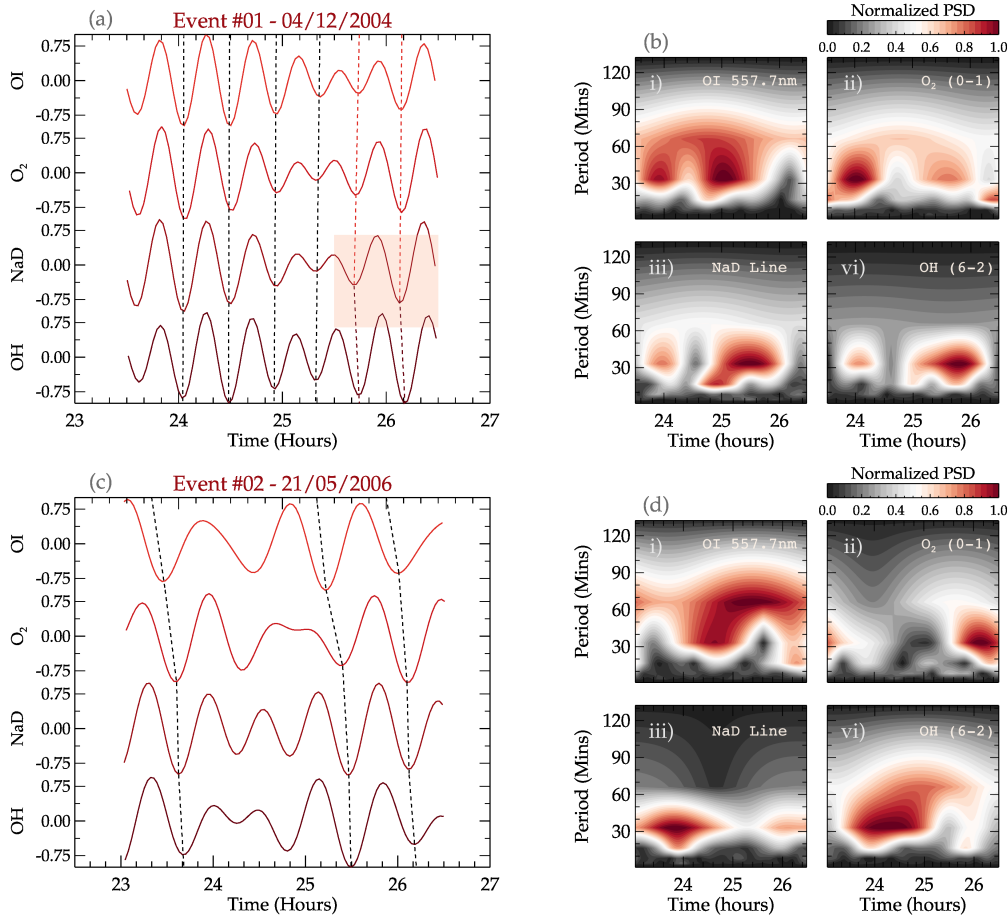
Figure 5. Observed upward and downward GW propagating events at São João do Cariri. In the upper panel, subpanels (a) and (b) the reconstructed downward propagating gravity waves of two periods on 04 December 2004 at OI 557.7 nm, O_2 (0-1), NaD line and OH (6-2) and their periods in each emission layer are presented. Similarly, the second case of an upward energy propagating gravity waves event of 21 May 2006 for the emission layers and their corresponding Wavelet analysis are shown in subpanels (c) and (d).

210   The periods determined in each emission layer using a Wavelet analysis are presented in Figure 5(b). In Figure 5(b.i), the spectrogram indicating the power spectral densities (PSD) relating the intensity of the periodicities of the wave to the time of occurrence for IO 557.7 nm emission layer is presented. The PSD for all the airglow emission layers has been normalized. The scale of the variations is defined by the color bar. A broad spectrum of high PSD intensity of the period was observed extending from 30 min to about 90 min throughout the entire observation window with a peak centered around 25 hrs. For the O_2 (0 - 1)

215   emission layer, the period has a strong PSD of period at 30 min, extending almost across the observation window. A narrow band of the period between 10 - 60 min with high PSD with a peak centered around 36 min was determined in the gravity

Table 1. Summary of the selected gravity waves events.

	Photometer			All-Sky Imager		Parameters		
	τ_z (min)	V_z (m/s)	λ_z (km)	τ_H (min)	k_H (m^{-1})	M_F (m^2/s^2)	E_p (J/kg)	E_k (J/kg)
Event #01								
$\tau_1(O_2)$	33.47	05.28	10.60	33.60	04.64×10^{-5}	01.07×10^{-2}	86.03	69.85
$\tau_1(OH)$						01.09×10^{-2}	87.91	107.50
Event #02								
$\tau_1(O_2)$	37.20	06.24	13.95	36.30	04.96×10^{-5}	04.50×10^{-2}	595.84	**.**
$\tau_1(OH)$						00.46×10^{-2}	60.93	**.**
$\tau_2(O_2)$	51.00	07.67	23.54	49.70	03.07×10^{-5}	02.72×10^{-2}	595.84	**.**
$\tau_2(OH)$						00.28×10^{-2}	60.93	**.**

wave oscillation through the NaD line and OH emission layers. The summary of the wave parameters of the photometers are presented in Table 1. Only the potential energy for Event #02 could be determined due to unavailability of observed winds. Hence, no estimated values for kinetic energy and subsequently total energy were presented in Table 1.

220   For event #02, their reconstructed GWs are presented in Figure 5(c and d) using the same standard of Figure 5(a and b). The dominant periods for these events are 00.62 hr (37.20 min) for all the emission layers and 00.88 hr (51.00 min) for O_2, NaD, and OH emission layers. The closest period to the second dominant period for OI 557.7 nm is 00.77 hr (46.20 min). According to the Wavelet analysis, the periods show a strong PSD from 20 - 60 min for O_2 and NaD line emission layers. For the OI 557.7 nm and OH (6 - 2) emission layers, the dominant periods extends to about 90 min.

225   5   Discussion

5.1   Phase Propagation

As presented in Section 4, two events with similar periods were selected. For Event #01, two dominant periods were detected, however, the first period present no phase change, implying it is possibly a ducted wave. For Event #02, the two dominant periods are within the gravity wave spectrum. In Figure 6, the phase leads and lags between the four emissions layers are
230   presented. To determine by how much a GWs with similar period propagating through the emission layers lags or leads the preceding or succeeding layers, the phase shifts are used.

5.1.1   Event #01

From the phases of the GWs of Event #01, OH leads NaD by 08.60 min, whereas NaD leads O_2 by 01.21 min. O_2 lags OI by 03.25 min. A consistent phase lead can be observed from OH through NaD to O2 except between O_2 and OI, where a phase
235   lag is observed. The phase lag observed between the emission layers of O_2 and OI was induced by the background wind due

to a shear. Despite this phase lag, the mean phase propagation of these GWs shows that OH leads OI by ∼06.58 min. Using this phase information and the period, Figure 6(a) is produced. Clearly, it is observed that the similar GW oscillation in the OH (red line) emission layer leads to the OI (green line) emission.

GWs propagation has been used to determine the energy propagation (Nyassor et al., 2018, and references therein). A
240 downward phase propagation implies upward energy propagation and vice versa. In the case of Event #01, the phase is upward; thus, the wave energy propagates downward. This indicates that this wave is generated upward and propagates downward. Downward propagating GWs, just like upward propagating waves, transport momentum and energy from the source location, thus depositing this momenta and energies wherever they break or dissipate. The subject of the characteristic of the momentum flux and total energy of the downward propagating GWs will be discussed in the subsequent section.
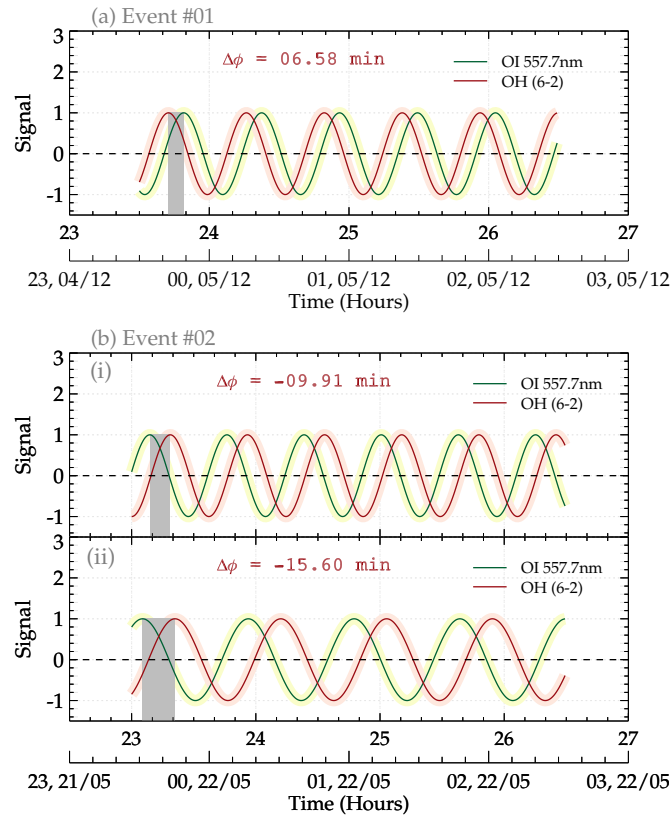
Figure 6. Two observed upward and downward propagating events at São João do Cariri. In panel (a), the phase difference is determined using the reconstructed signal of O_2 (0 - 1) and OH (6 - 2) for Event #01. Using the reconstructed signal for each period in Event #02, the phase differences between O_2 (0-1) and OH (6-2) are determined and presented in panel (b).

5.1.2 Event #02

$\tau_H = 37.20 \, \text{min}$

For Event #02, propagation of the GW with $\tau = 37.20$ min shows a downward phase propagation with altitude. Here, OH lags the NaD line by 09.46 min, NaD leads O_2 by 08.74 sec, and O_2 lags OI by 35 secs. In general, it was found that OH lags OI for an average of 9.91 min. Comparing the signal in Figure 6(b.i), a clear phase lag was observed between OH (red solid line) and OI (green solid line) emission layers. In Figure 6(b.i), the phase difference ($\Delta\phi$) between OH and OI is represented by a negative ($-$) value to indicate a lag.

$\tau_H = 51.11 \, \text{min}$

The second dominant period of Event #02 demonstrated a consistent lag in the phase propagation from OH through NaD and O_2 to OI emission layers, clearly showing an upward phase propagation. OH was found to lag NaD by 04.39 min, whereas NaD lags O2 by 08.33 min, and O2 lags OI by 02.97 min. This lagging phase propagation nature of this period is shown in subpanel (ii) of Figure 6. Similarly, the $\Delta\phi$ is negative due to the phase lag. As shown, both GWs in Event #02 are upward propagating GWs; thus, they are transporting momentum from the lower to the upper atmosphere.

6 Momentum Flux and Wave Energy

Gravity waves transport energy from their excitation/source location to their sink (dissipation/breaking), whether the waves are upward or downward propagating (Fritts and Alexander, 2003; Vadas et al., 2009; Nyassor et al., 2021). The amplitude of upward propagating GWs grows due to the decreasing density with increasing altitude. So, for a downward propagating wave, the amplitude of the wave may suffer amplitude decrease due to increasing density with decreasing altitude. In Section 5.1, two GW events are selected with a downward and an upward phase propagation. The phases analysis in Figure 6 further showed phase leads and lags. Even though Event #01 (the upward phase propagation), showed small phase shifts, the individual reconstructed signal using the wave phases and periods affirms the phase difference between OI 557.7 nm and OH (6-2). Similarly, the individual periods for Event #02 reconstructed in Figure 7(a and b) confirmed downward phase propagations.

According to Vadas (2007), diffusion processes inhibit the propagation of GWs where molecular viscosity and thermal diffusivity are significant in the upper mesosphere and lower thermosphere. Eddy diffusion is also known as a significant process that inhibits gravity wave propagation in the lower and middle atmosphere (Yiğit and Medvedev, 2016). However, high-frequency GWs mostly survive these conditions and are capable of propagating to the upper atmosphere, where they break or dissipate. Therefore, in the case where no or little wave breaking/dissipation occurs, what will be the characteristics of the GWs momentum and energy for an upward and downward propagating? These features are explored using the momentum flux and energy of the GWs selected at O_2 and OH (6 - 2) emission layers, using their rotational temperature.

6.1 Event #01

275 The momentum and energy variation with time (and averages) at the O_2 and OH (6 - 2) emission is presented in Figure 7 for the GW event of 04 December 2004 (Event #01). Note that the same periods determined in the intensity of the four emissions were determined in the rotational temperatures of the O_2 and OH (6 - 2). In Figure 7(a), the estimated momentum flux at the altitudes of O_2 (black line) emission layer and OH (6 - 2) (red line) emission layer is shown. The time averages of the momentum fluxes for O_2 and OH (6 - 2) indicated that $M_{F(O_2)}$ is lesser than $M_{F(OH)}$. For the potential energy E_p for each respective emission

280 layer, the potential energy at the OH (6 - 2) emission layer surpasses that of O_2. Similarly, the kinetic (E_k) and total (E_T) energies in panels panels (c) and (d), respectively, showed the same characteristics as the E_p.
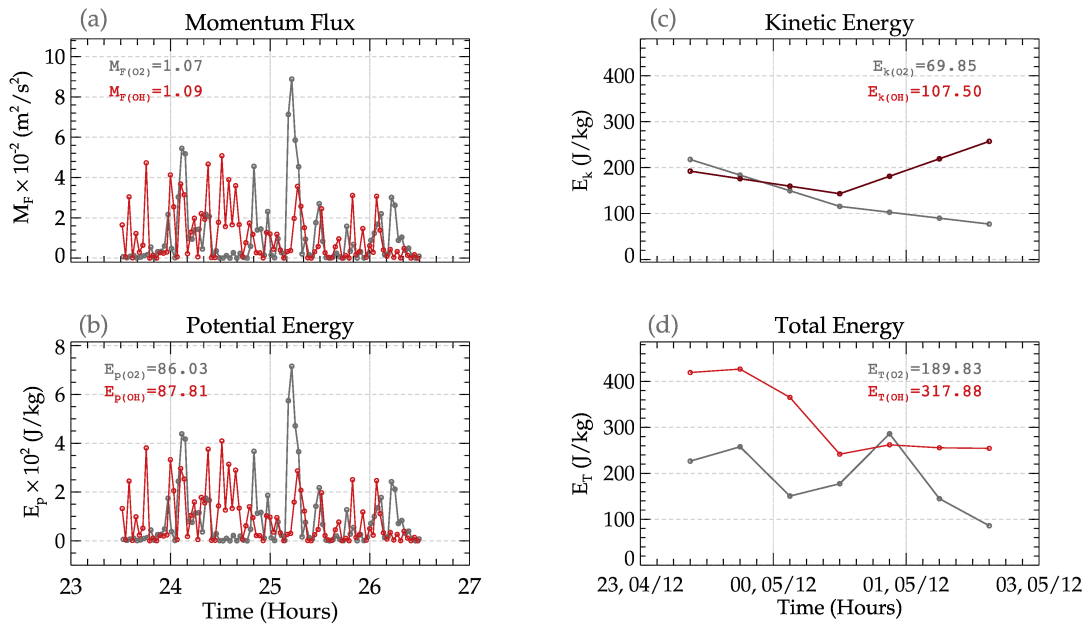
Figure 7. The characteristics of momentum flux (a), potential (b), kinetic (c), and total (c) energies at the O_2 and OH (6-2) emission altitudes for the event of 04 December 2004.

6.2 Event #02

Similar to Event #01, the momentum flux and potential energy at each emission layer for the two GWs observed in the event of 21 May 2006 is presented in Figure 8. However, for this event, the kinetic energy and, subsequently, the total energy could not

285 be estimated due to unavailability of observed wind data. Since this current study focuses on the momentum flux characteristics, a discussion of the momentum flux and the potential energy can still give the relevant insight intended for the work. In panel (a), the momentum flux for the first period (τ = 37.20 min) is presented, whereas in panel (b), the momentum flux of the second period (τ = 51.00 min) is presented. The momentum flux for both periods in this event is presented in panel (c), since the potential energy estimation depends on the temperature.
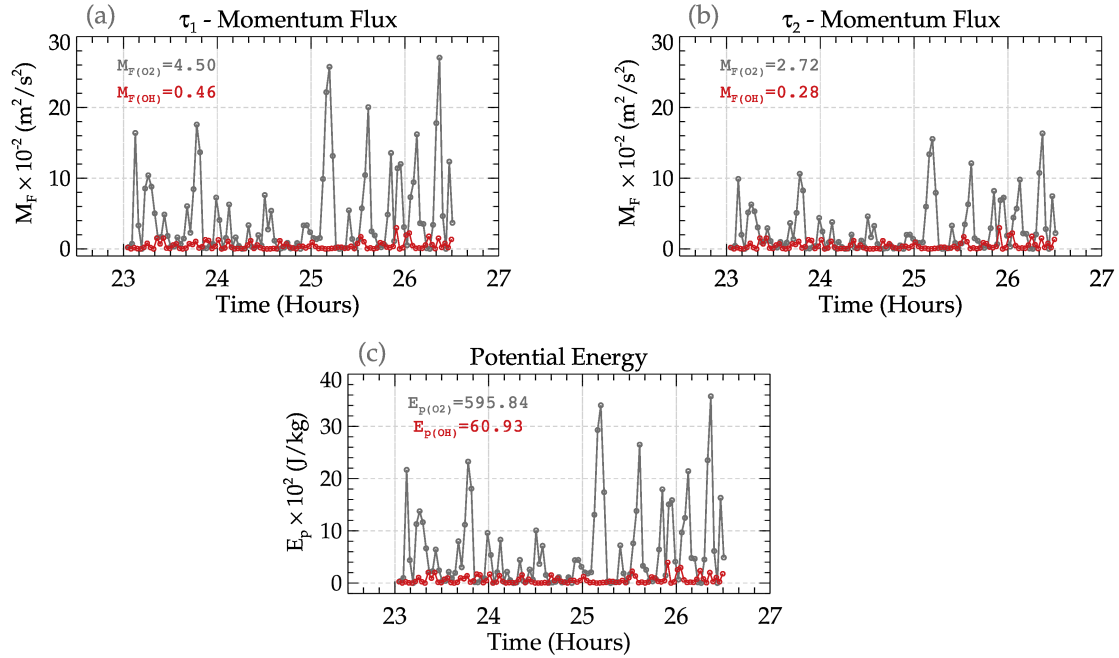
Figure 8. The characteristics of momentum flux of $\tau = 37.20\,\mathrm{min}$ (a), $\tau = 51.00\,\mathrm{min}$ (b), and total potential energy (d) energy at the O_2 and OH (6-2) emission altitudes for the event of 21 May 2006.

Comparison between the momentum fluxes at O_2 and OH (6-2) emission layers for this event showed a vast difference in the momentum fluxes. The M_F at the O_2 is much higher than that of OH (6-2) This difference is attributed to the large amplitude of the gravity wave perturbations in the O_2 temperature residual since the estimation of the potential energy and the momentum flux depend on the temperature residual. Another explanation for this difference can be attributed to an increase in amplitude due to a decrease in density with altitude since these GWs are propagating upward.

Comparison between the two events showed that regardless of whether GWs propagate upward or downward, momentum and energy are transported from the source to the sink. It is imperative to say that the momentum and energy at the source will be less. This has clearly been demonstrated in these two selected events, attesting to the fact that atmospheric density significantly impacts the amplitude, momentum, and energy. Using Lidar temperature profile, Kaifler et al. (2017) studied the dynamics of downward propagating gravity waves. They observed that one third of the momentum flux is carried by the downward propagating GW from 85 km altitude to a lower altitude. In this recent case, only a small fraction of the wave energy was transported. A great amount of the wave energy was observed to be transported by the upward propagating wave. Considering the fact that the vertical propagation of these GWs are only within a 5 km range, the full extent of the characteristics cannot be explored due to the data set being unavailable. The total energy of Event #01 also depicted characteristics similar to the potential energy. Similar behavior of the potential energy is also observed in the characteristics of the momentum flux, indicating the theory governing the transport of momentum and energy by atmospheric GWs. Using a longer altitude range and

high temporal resolution lidar data, for instance, this subject can be explored in detail such that standards can be defined so as to determined the signatures of vertical propagating GWs due to reflection and non-primary GWs.

7 Conclusions

This paper studies the characteristic dynamics of momentum flux and energy of both upward and downward propagating GWs
310 using an event each selected for case study. Using the phase propagation of GWs with almost the same period through the emission layers of OI 557.7 nm, O_2 (0-1), NaD-line, and OH (6-2), the vertical propagation of the waves was determined. Using the ratio of the altitude difference (Δd) to the phase difference ($\Delta \phi$), the vertical phase speed and, consequently, the wavelength were estimated. From the phase propagation, an event each of a downward and an upward propagating GWs was selected for further studies.

315 For each case, the potential energy and momentum flux were estimated, and their characteristics were studied. For the downward propagating GWs, it was determined that the potential, kinetic, and total energies at the O_2 emission altitudes were lower than those at OH emission altitudes. The upward propagating wave (second event) showed distinct characteristics in the potential energy and momentum fluxes for the two period GWs in this event. The momentum flux and the potential energy at the OH emission altitude are far lower than that of the momentum flux at the O_2 emission layer. These characteristics indicate
320 the growth in the amplitude of GW with increasing altitude and decreasing density. The significant growth in the amplitude of the GW perturbation in the O_2 rotational temperature affirms this theory. As mentioned, there was little or no amplitude growth in the GW perturbations of O_2 and OH (9 - 2) rotational temperature of event #01. This was attributed to the increasing density with decreasing altitude, possibly inhibiting amplitude growth.

This work, however, is limited to only a 5 km range of altitude, that is, only in the mesopause region, hence to come to a
325 definite conclusion that can be used to set boundary conditions for upward and downward GW propagation scenarios, a companion study is intended to be conducted using Lidar data and other co-located observations. However, this work demonstrated differences in the dynamics of the momentum and energy of downward and upward propagating GWs.

Appendix A

A1 Determination of kinetic energy (E_k) and momentum flux (M_F) of gravity waves

330 In Figure A1, the zonal and meridional winds are presented in panels (a) and (b) are presented. The corresponding GWs perturbations, u' and v' in the zonal and meridional winds, are presented in panels (c) and (d).
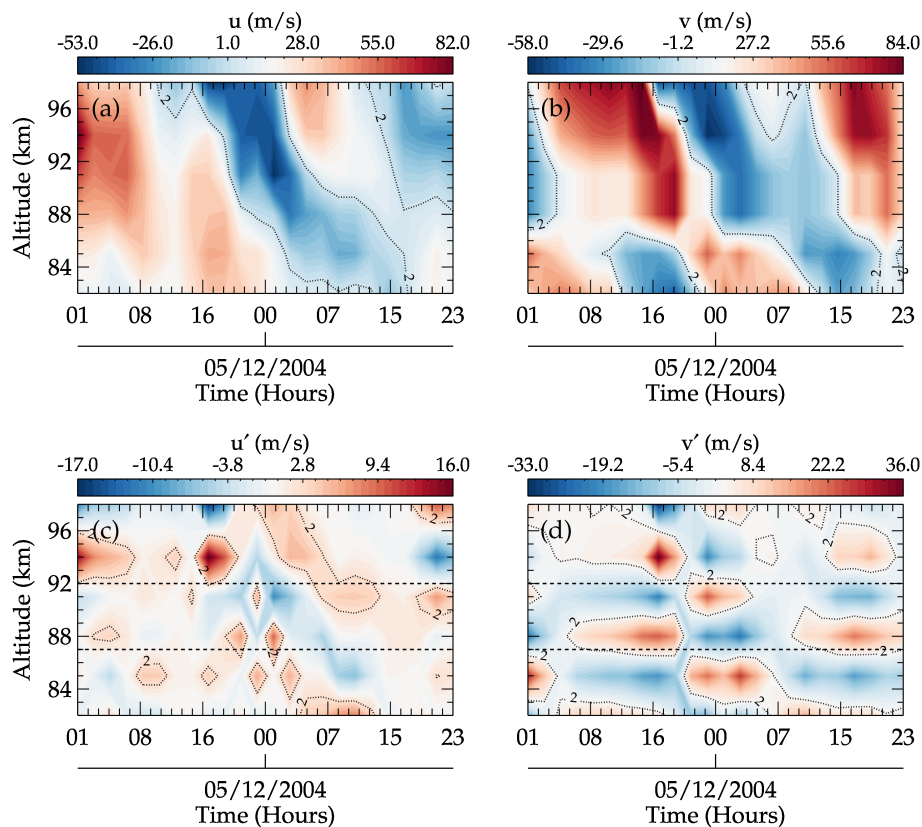
Figure A1. Meteor radar winds during the December 4, 2004 gravity wave (GW) event at São João do Cariri. The zonal and meridional winds are presented in the panels (a) and (b) with their corresponding GWs perturbations in panels (c) and (d).

The kinetic energy is derived from Equation 4. The results of the winds and GW induced wind perturbations for the entire 04 - 05 December 2004 are presented in a contour plot due to the nature of the wind data. This is done to obtain the general characteristics of the estimated parameter. The meteor radar wind has a vertical and temporal resolutions of 1 km and 1 hr

335 respectively. As a result, the data is interpolated to obtain 0.5 km and 1 hour resolution.

A2 Spectral and Keogram Analysis

Spectral analysis is used to preprocess the original all-sky airglow images according to the procedure of Wrasse et al. (2024). Next, a Fast Fourier Transform based keogram analysis described in Figueiredo et al. (2018) is then used to obtain the result presented in A2.
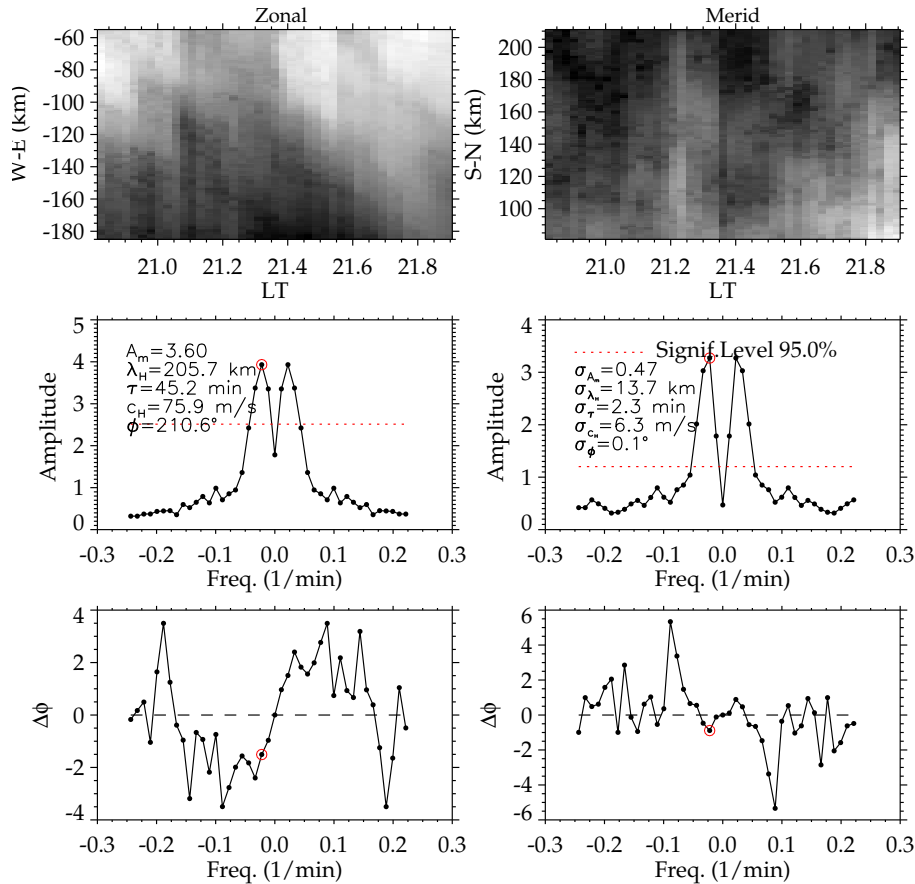
Figure A2. Result of OH emission layer keogram analysis of Event #02 with period of $\tau = 49.70\,\text{min}$

340   In the upper panel, (the left side) is the zonal keogram, whereas the right side is the meridional (merid) keogram. These keograms correspond to the selected region with GWs perturbations. The middle panel is the amplitude (left) with the GW parameters listed and their corresponding standard deviation (σ) in the middle right panel. The red dotted horizontal lines indicate a significant level greater than 95.0%, whereas the red circle with a black dot shows the peak amplitude. The lower panels represent the phase difference in the zonal (left) and meridional (right) components of the waves. The GW characteristics
345   in the middle panel are the horizontal parameters (i.e., the sum of the zonal and meridional components).

Author contributions. PKN wrote the article and performed most of the analysis. CMW assisted in the validation of the methodologies and in the revision of the manuscript. IP assisted in the validation of the some methodologies and in the revision of the manuscript. CAOBF assisted in the development and validation of some of the methodologies and the revision of the manuscript. RAB provided the photometer an meteor radar data. HT revised the manuscript, and GAG helped in the validation of some of the methodologies and the revision of the manuscript.

Competing interests. The contact author has declared that none of the authors has any competing interests.

Acknowledgements. Prosper K. Nyassor acknowledge the support of Fundação de Amparo à Pesquisa do Estado de São Paulo (FAPESP). Cristiano M. Wrasse thanks the Coordenação de Aperfeiçoamento de Pessoal de Nível Superior (CAPES) and the Conselho Nacional de Desenvolvimento Científico e Tecnológico (CNPq) for the support. Thanks are given to the Brazilian Ministry of Science, Technology and Innovations (MCTI) and the Brazilian Space Agency (AEB). Cosme A. O. B. Figueiredo acknowledges FAPESP and the Fundação de apoio à pesquisa do estado da Paraíba. The authors thank the Estudo e Monitoramento Brasileiro do Clima Espacial (EMBRACE/INPE) for the provision of all-sky.

References

Bageston, J., Wrasse, C. M., Batista, P., Hibbins, R., Fritts, D., Gobbi, D., and Andrioli, V.: Observation of a mesospheric front in a thermal-doppler duct over King George Island, Antarctica, https://doi.org/10.5194/acp-11-12137-2011, 2011.

Becker, E. and Schmitz, G.: Climatological Effects of Orography and Land–Sea Heating Contrasts on the Gravity Wave–Driven Circulation of the Mesosphere, Journal of the Atmospheric Sciences, 60, 103 – 118, https://doi.org/10.1175/1520-0469(2003)060<0103:CEOOAL>2.0.CO;2, 2003.

Buriti, R., Takahashi, H., and Gobbi, D.: First results from mesospheric airglow observations at 7.5 º S., Revista Brasileira de Geofísica, 19, 169–176, 2001.

Chou, M. Y., Lin, C. C., Yue, J., Tsai, H. F., Sun, Y. Y., Liu, J. Y., and Chen, C. H.: Concentric traveling ionosphere disturbances triggered by Super Typhoon Meranti (2016), Geophysical Research Letters, 44, 1219–1226, https://doi.org/doi:10.1002/2016GL072205, 2017.

Figueiredo, C., Takahashi, H., Wrasse, C., Otsuka, Y., Shiokawa, K., and Barros, D.: Investigation of nighttime MSTIDS observed by optical thermosphere imagers at low latitudes: Morphology, propagation direction, and wind filtering, Journal of Geophysical Research: Space Physics, 123, 7843–7857, https://doi.org/https://doi.org/10.1029/2018JA02543, 2018.

Figueiredo, C., Vadas, S., Becker, E., Wrasse, C., Takahashi, H., Nyassor, P., and Barros, D.: Secondary gravity waves from the Tonga volcano eruption: Observation and modeling over New Zealand and Australia, Journal of Geophysical Research: Space Physics, 128, e2023JA031 476, 2023.

Fritts, D. C. and Alexander, M. J.: Gravity wave dynamics and effects in the middle atmosphere, Reviews of geophysics, 41, https://doi.org/10.1029/2001RG000106, 2003.

Gossard, E. E. and Hooke, W. H.: Waves in the atmosphere: atmospheric infrasound and gravity waves-their generation and propagation, Atmospheric Science, 2, 1975.

Heale, C. and Snively, J.: Gravity wave propagation through a vertically and horizontally inhomogeneous background wind, Journal of Geophysical Research: Atmospheres, 120, 5931–5950, https://doi.org/10.1002/2015JD023505, 2015.

Heale, C. J., Bossert, K., Vadas, S. L., Hoffmann, L., Dörnbrack, A., Stober, G., Snively, J., and Jacobi, C.: Secondary gravity waves generated by breaking mountain waves over Europe, Journal of Geophysical Research: Atmospheres, 125, e2019JD031 662, https://doi.org/10.1029/2019JD031662, 2020.

Holton, J. R.: The role of gravity wave induced drag and diffusion in the momentum budget of the mesosphere, Journal of Atmospheric Sciences, 39, 791–799, https://doi.org/10.1175/1520-0469(1982)039<0791:TROGWI>2.0.CO;2, 1982.

Kaifler, N., Kaifler, B., Ehard, B., Gisinger, S., Dörnbrack, A., Rapp, M., Kivi, R., Kozlovsky, A., Lester, M., and Liley, B.: Observational indications of downward-propagating gravity waves in middle atmosphere lidar data, Journal of Atmospheric and Solar-Terrestrial Physics, 162, 16–27, 2017.

Le Du, T., Keckhut, P., Hauchecorne, A., and Simoneau, P.: Observation of gravity wave vertical propagation through a mesospheric inversion layer, Atmosphere, 13, 1003, https://doi.org/10.3390/atmos13071003, 2022.

Li, Q., Xu, J., Liu, H., Liu, X., and Yuan, W.: How do gravity waves triggered by a typhoon propagate from the troposphere to the upper atmosphere?, Atmospheric Chemistry and Physics, 22, 12 077–12 091, https://doi.org/10.5194/acp-22-12077-2022, 2022.

Lindzen, R.: Gravity waves in the mesosphere, Dynamics of the middle atmosphere, pp. 3–18, 1984.

Lindzen, R. S.: Turbulence and stress owing to gravity wave and tidal breakdown, Journal of Geophysical Research: Oceans, 86, 9707–9714, https://doi.org/https://doi.org/10.1029/JC086iC10p09707, 1981.

395   Mies, F. H.: Calculated vibrational transition probabilities of OH (X2Π), Journal of Molecular Spectroscopy, 53, 150–188, 1974.

Nappo, C. J.: An introduction to atmospheric gravity waves, Academic press, 2013.

Nyassor, P. K., Buriti, R. A., Paulino, I., Medeiros, A. F., Takahashi, H., Wrasse, C. M., and Gobbi, D.: Determination of gravity wave parameters in the airglow combining photometer and imager data, in: Annales Geophysicae, vol. 36, pp. 705–715, Copernicus GmbH, https://doi.org/10.5194/angeo-36-705-2018, 2018.

400   Nyassor, P. K., Wrasse, C. M., Gobbi, D., Paulino, I., Vadas, S. L., Naccarato, K. P., Takahashi, H., Bageston, J. V., Figueiredo, C. A. O. B., and Barros, D.: Case Studies on Concentric Gravity Waves Source Using Lightning Flash Rate, Brightness Temperature and Backward Ray Tracing at São Martinho da Serra (29.44°S, 53.82°W), Journal of Geophysical Research: Atmospheres, 126, e2020JD034 527, https://doi.org/https://doi.org/10.1029/2020JD034527, 2021.

Nyassor, P. K., Wrasse, C. M., Paulino, I., Gobbi, D., Yiğit, E., Takahashi, H., Batista, P. P., Naccarato, K. P., Buriti, R. A., Paulino, A. R.,
405   Barros, D., and Figueiredo, C. A. O. B.: Investigations on Concentric Gravity Wave Sources Over the Brazilian Equatorial Region, Journal of Geophysical Research: Atmospheres, 127, e2021JD035 149, https://doi.org/https://doi.org/10.1029/2021JD035149, 2022a.

Nyassor, P. K., Wrasse, C. M., Paulino, I., São Sabbas, E. F., Bageston, J. V., Naccarato, K. P., Gobbi, D., Figueiredo, C. A., Ayorinde, T. T., Takahashi, H., et al.: Sources of concentric gravity waves generated by a moving mesoscale convective system in southern Brazil, Atmospheric Chemistry and Physics, 22, 15 153–15 177, https://doi.org/10.5194/acp-22-15153-2022, 2022b.

410   Paulino, I., Figueiredo, C. A. O. B., Rodrigues, F. S., Buriti, R. A., Wrasse, C. M., Paulino, A. R., Barros, D., Takahashi, H., Batista, I. S., Medeiros, A. F., Batista, P. P., Abdu, M. A., de Paula, E. R., Denardini, C. M., Lima, L. M., Cueva, R. Y., and Makela, J. J.: Atmospheric Gravity Waves Observed in the Nightglow Following the 21 August 2017 Total Solar Eclipse, Geophysical Research Letters, 47, e2020GL088 924, https://doi.org/https://doi.org/10.1029/2020GL088924, 2020.

Sato, K. and Yoshiki, M.: Gravity wave generation around the polar vortex in the stratosphere revealed by 3-hourly radiosonde observations
415   at Syowa Station, Journal of the Atmospheric Sciences, 65, 3719–3735, https://doi.org/10.1175/2008JAS2539.1, 2008.

Schöch, A., Baumgarten, G., Fritts, D., Hoffmann, P., Serafimovich, A., Wang, L., Dalin, P., Müllemann, A., and Schmidlin, F.: Gravity waves in the troposphere and stratosphere during the MaCWAVE/MIDAS summer rocket program, Geophysical research letters, 31, https://doi.org/10.1029/2004GL019837, 2004.

Sentman, D., Wescott, E., Picard, R., Winick, J., Stenbaek-Nielsen, H., Dewan, E., Moudry, D., Sao Sabbas, F., Heavner, M., and Morrill,
420   J.: Simultaneous observations of mesospheric gravity waves and sprites generated by a midwestern thunderstorm, Journal of Atmospheric and Solar-Terrestrial Physics, 65, 537–550, https://doi.org/10.1016/S1364-6826(02)00328-0, 2003.

Silverman, S.: Night airglow phenomenology, Space Science Reviews, 11, 341–379, 1970.

Sivjee, G. and Hamwey, R.: Temperature and chemistry of the polar mesopause OH, Journal of Geophysical Research: Space Physics, 92, 4663–4672, 1987.

425   Snively, J. B. and Pasko, V. P.: Excitation of ducted gravity waves in the lower thermosphere by tropospheric sources, Journal of Geophysical Research: Space Physics, 113, https://doi.org/10.1029/2007JA012693, 2008.

Snively, J. B., Pasko, V. P., Taylor, M. J., and Hocking, W. K.: Doppler ducting of short-period gravity waves by midlatitude tidal wind structure, Journal of Geophysical Research: Space Physics, 112, https://doi.org/10.1029/2006JA011895, 2007.

Suzuki, S., Lübken, F.-J., Baumgarten, G., Kaifler, N., Eixmann, R., Williams, B. P., and Nakamura, T.: Vertical propagation of a
430   mesoscale gravity wave from the lower to the upper atmosphere, Journal of Atmospheric and Solar-Terrestrial Physics, 97, 29–36, https://doi.org/10.1016/j.jastp.2013.01.012, 2013.

Takahashi, H., Batista, P. P., Buriti, R., Gobbi, D., Nakamura, T., Tsuda, T., and Fukao, S.: Simultaneous measurements of airglow oh emissionand meteor wind by a scanning photometer and the muradar, Journal of atmospheric and solar-terrestrial physics, 60, 1649–1668, 1998.

435 Taori, A., Taylor, M. J., and Franke, S.: Terdiurnal wave signatures in the upper mesospheric temperature and their association with the wind fields at low latitudes (20 N), Journal of Geophysical Research: Atmospheres, 110, https://doi.org/10.1029/2004JD004564, 2005.

Taylor, M. J. and Hapgood, M.: Identification of a thunderstorm as a source of short period gravity waves in the upper atmospheric nightglow emissions, Planetary and space science, 36, 975–985, https://doi.org/10.1016/0032-0633(88)90035-9, 1988.

Townsend, A.: Internal waves produced by a convective layer, Journal of Fluid Mechanics, 24, 307–319,
440 https://doi.org/10.1017/S0022112066000661, 1966.

Vadas, S. L.: Horizontal and vertical propagation and dissipation of gravity waves in the thermosphere from lower atmospheric and thermospheric sources, Journal of Geophysical Research: Space Physics, 112, https://doi.org/10.1029/2006JA011845, 2007.

Vadas, S. L., Fritts, D. C., and Alexander, M. J.: Mechanism for the generation of secondary waves in wave breaking regions, Journal of the Atmospheric Sciences, 60, 194–214, https://doi.org/10.1175/1520-0469(2003)060<0194:MFTGOS>2.0.CO;2, 2003.

445 Vadas, S. L., Taylor, M. J., Pautet, P.-D., Stamus, P., Fritts, D. C., Liu, H.-L., São Sabbos, F., Batista, V., Takahashi, H., and Rampinelli, V.: Convection: the likely source of the medium-scale gravity waves observed in the OH airglow layer near Brasilia, Brazil, during the SpreadFEx campaign, in: Annales Geophysicae, vol. 27, p. 231, European Geosciences Union, https://doi.org/10.5194/angeo-27-231-2009, 2009.

Vargas, F., Gobbi, D., Takahashi, H., and Lima, L.: Gravity wave amplitudes and momentum fluxes inferred from OH airglow intensities and
450 meteor radar winds during SpreadFEx, in: Annales Geophysicae, vol. 27, pp. 2361–2369, Copernicus Publications Göttingen, Germany, 2009.

Wang, L. and Geller, M. A.: Morphology of gravity-wave energy as observed from 4 years (1998–2001) of high vertical resolution US radiosonde data, Journal of Geophysical Research: Atmospheres, 108, 2003.

Wrasse, C. M., Takahashi, H., and Gobbi, D.: Comparison of the OH (8-3) and (6-2) band rotational temperature of the mesospheric airglow
455 emissions, Revista Brasileira de Geofísica, 22, 223–231, https://doi.org/10.1590/S0102-261X2004000300002, 2004.

Wrasse, C. M., Nyassor, P. K., da Silva, L. A., Figueiredo, C. A., Bageston, J. V., Naccarato, K. P., Barros, D., Takahashi, H., and Gobbi, D.: Studies on the propagation dynamics and source mechanism of quasi-monochromatic gravity waves observed over São Martinho da Serra (29° S, 53° W), Brazil, Atmospheric Chemistry and Physics, 24, 5405–5431, 2024.

Yamashita, C., Chu, X., Liu, H.-L., Espy, P. J., Nott, G. J., and Huang, W.: Stratospheric gravity wave characteristics and sea-
460 sonal variations observed by lidar at the South Pole and Rothera, Antarctica, Journal of Geophysical Research: Atmospheres, 114, https://doi.org/10.1029/2008JD011472, 2009.

Yiğit, E. and Medvedev, A. S.: Role of gravity waves in vertical coupling during sudden stratospheric warmings, Geoscience Letters, 3, 1–13, https://doi.org/https://doi.org/10.1186/s40562-016-0056-1, 2016.

Yue, J., Vadas, S. L., She, C.-Y., Nakamura, T., Reising, S. C., Liu, H.-L., Stamus, P., Krueger, D. A., Lyons, W., and Li, T.: Concentric
465 gravity waves in the mesosphere generated by deep convective plumes in the lower atmosphere near Fort Collins, Colorado, Journal of Geophysical Research: Atmospheres, 114, https://doi.org/10.1029/2008JD011244, 2009.

Yue, J., Miller, S. D., Straka III, W. C., Noh, Y.-J., Chou, M.-Y., Kahn, R., and Flower, V.: La Soufriere volcanic eruptions launched gravity waves into Space, Geophysical Research Letters, 49, e2022GL097 952, https://doi.org/10.1029/2022GL097952, 2022.